

# MULTI-MODEL ENSEMBLE ANALYSIS WITH NEURAL NETWORK GAUSSIAN PROCESSES

BY TREVOR HARRIS<sup>1,\*</sup>, BO LI<sup>2</sup> AND RYAN SRIVER<sup>3</sup>

<sup>1</sup>Department of Statistics, Texas A&M University, \*[tharris@tamu.edu](mailto:tharris@tamu.edu)

<sup>2</sup>Department of Statistics, University of Illinois at Urbana Champaign, [libo@illinois.edu](mailto:libo@illinois.edu)

<sup>3</sup>Department of Atmospheric Sciences, University of Illinois at Urbana Champaign, [rsriver@illinois.edu](mailto:rsriver@illinois.edu)

Multi-model ensemble analysis integrates information from multiple climate models into a unified projection. However, existing integration approaches based on model averaging can dilute fine-scale spatial information and incur bias from rescaling low-resolution climate models. We propose a statistical approach, called NN-GPR, using Gaussian process regression (GPR) with an infinitely wide deep neural network based covariance function. NN-GPR requires no assumptions about the relationships between models, no interpolation to a common grid, no stationarity assumptions, and automatically downscales as part of its prediction algorithm. Model experiments show that NN-GPR can be highly skillful at surface temperature and precipitation forecasting by preserving geospatial signals at multiple scales and capturing inter-annual variability. Our projections particularly show improved accuracy and uncertainty quantification skill in regions of high variability, which allows us to cheaply assess tail behavior at a  $0.44^\circ/50$  km spatial resolution without a regional climate model (RCM). Evaluations on reanalysis data and SSP245 forced climate models show that NN-GPR produces similar, overall climatologies to the model ensemble while better capturing fine scale spatial patterns. Finally, we compare NN-GPR's regional predictions against two RCMs and show that NN-GPR can rival the performance of RCMs using only global model data as input.

**1. Introduction.** Climate models are central to modern climate science and are the primary tool for projecting future climate states (Flato et al., 2014). However, constructing climate models is an international effort, with various modeling centers developing distinct models semi-independently. This situation has led to a large number of plausible, though disagreeing, models all representing the same earth system (Knutti et al., 2010; Flato et al., 2014). Rather than select a “best” climate model, climate scientists incorporate many models into multi-model ensembles, which are then combined or integrated into a consensus estimate. Model integrations often show improved reconstruction skill compared to the individual models (Lambert and Boer, 2001; Gleckler, Taylor and Doutriaux, 2008; Knutti et al., 2010). Ensembles also allow climate scientists to quantify uncertainty through inter-model variability. For example, initial condition ensembles sample internal variability, perturbed physics ensembles sample uncertainties in parameters, and multi-model ensembles such as CMIP sample forcing uncertainties, structural model differences, and initial conditions (Sansom, Stephenson and Bracegirdle, 2017).

Properly integrating multi-model ensembles into a consensus estimate has been the topic of much discussion (Tebaldi and Knutti, 2007). By far, the most common and convenient approach is to average all models into a pointwise ensemble mean (Flato et al., 2014) and to use the pointwise inter-model variability as the projection uncertainty. Averaging can be done

---

*Keywords and phrases:* multi-model ensembles, climate model integration, Gaussian process regression, deep learning.

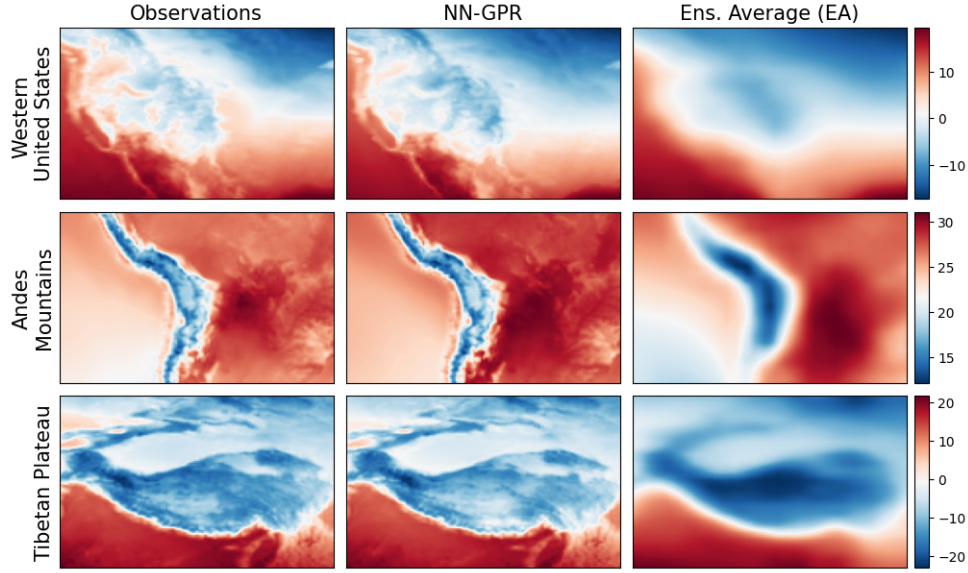


FIG 1. Observations and model predictions using the proposed method (NN-GPR) and a naive ensemble average (EA). EA shows the characteristic blurring caused by model weighting, while NN-GPR provides highly detailed projections even within small regions. EA is of limited use at the regional scale, leading to expensive regional climate model (RCMs) replacements. In contrast, NN-GPR's projections do not require further refinement via RCMs and downscaling. Temperature scales in  $^{\circ}\text{C}$ .

either democratically, whereby each model receives the same weight or with weights based on model skill, reliability, and inter-model dependence (Giorgi and Mearns, 2002, 2003; Abramowitz et al., 2019). This type of model integration is known as ensemble averaging or weighted ensemble averaging.

A fundamental challenge with ensemble averaging is how to gain the benefits of a model average without losing individual model skill, i.e., while retaining inter-annual variability and spatial information. In the extreme case, simple model averaging may cause severe blurring that erodes nearly all spatial signals (Figure 1). This drawback has spurred many alternative approaches based on reliability weighting, Bayesian hierarchical models, regression, and machine learning that all use observational data to improve model integration.

Bayesian methods assume a statistical model for the actual climate and use the climate models and observations to learn the parameters of the statistical model (Tebaldi et al., 2004; Smith et al., 2009; Bhat et al., 2011; Rougier, Goldstein and House, 2013; Sansom, Stephenson and Bracegirdle, 2017; Bowman et al., 2018). Bayesian approaches differ significantly from ensemble averaging methods in incorporating model variability to describe the actual climate. Instead of linearly combining models or picking a subset to combine linearly, Bayesian models quantify different sources of variability (e.g., model uncertainty, model inadequacy, and natural variability) and learn posterior estimates from the climate model ensembles. As a result, the posterior estimates can rigorously quantify prediction uncertainty and make distributional forecasts. Bayesian methods can also learn more complex, emergent relationships than simple linear combinations (Chandler (2013); Sansom, Stephenson and Bracegirdle (2017).

Regression (Räisänen, Ruokolainen and Ylhäisi, 2010; Bracegirdle and Stephenson, 2012) and machine learning methods (Ghafarianzadeh and Monteleoni, 2013) learn a mapping from the climate model ensemble, or the ensemble mean, to the target climate process. These prediction oriented methods often show superior predictive skill compared to ensemble averaging (Greene, Goddard and Lall, 2006). However, they can be computationally expensive

and may fail to generalize to future climate scenarios if the distribution of the climate models changes significantly from the training period. Additionally, linear regression strongly assumes that the actual climate system is a simple linear combination of model output.

Instead, we propose a nonparametric approach and use Gaussian process regression (GPR) (Rasmussen and Williams, 2006) to combine climate models. We use the recently developed deep neural network kernel functions (Lee et al., 2017; Garriga-Alonso, Rasmussen and Aitchison, 2018) to define a GPR model, called NN-GPR, from climate model ensembles to reanalysis fields that exactly reproduces the predictions of an infinitely wide deep neural network. GPR combines the strengths of Bayesian methods and prediction methods into a fundamentally new approach for highly flexible model integration.

Our approach requires no assumptions about the relationships between models, no interpolation to a common grid, and is computationally efficient at our sample sizes. Additionally, NN-GPR has only three parameters yet still allows for non-linear and dynamically evolving predictions, which we show can outperform existing averaging and regression approaches. We show that our approach can preserve geospatial characteristics beyond the capabilities of previous methods and thus act as a simultaneous forecasting and pattern scaling technique (Figure 1) comparable to regional climate models (RCMs). By using low resolution model output to capture high resolution patterns, we partially mitigate the high computational cost of RCM ensembling while still capturing extreme behavior through the posterior predictive distributions.

**2. Background.** Our proposed approach is a Gaussian process regression (GPR) model (Rasmussen and Williams, 2006), a type of Bayesian nonparametric regression. We briefly review GPR and the recently developed deep neural network kernels (NNGP) (Lee et al., 2017; Garriga-Alonso, Rasmussen and Aitchison, 2018). NNGP kernels provide great flexibility to define GPRs that inherit much of the power of deep learning at a significantly reduced computational cost on smaller sample sizes. These flexible kernels are, therefore ideal for learning complex functions from high dimensional vectors (climate field output) to high dimensional vectors (reanalysis data) with limited training data (Arora et al., 2019).

**2.1. Gaussian process regression.** Let  $\mathcal{X} \subset \mathbb{R}^q$ ,  $\mathcal{Y} \subset \mathbb{R}^d$  be vector spaces and let  $D = \{(X_t, Y_t)\}_{t=1}^n$  represent a dataset of  $n$  paired observations  $(X_t, Y_t) \in \mathcal{X} \times \mathcal{Y}$ . In this section, we assume  $d = 1$ , although our model in Section 3 assumes  $d \geq 1$  so that for example,  $X_t$  can be a climate model ensemble and  $Y_t$  can be a reanalysis field. A Gaussian process ( $\mathcal{GP}$ ) is an infinite collection of random variables, such that any finite sub-collection has a joint Gaussian distribution (Rasmussen and Williams, 2006). We can define a  $\mathcal{GP}$  distribution over random functions  $f : \mathcal{X} \mapsto \mathcal{Y}$  by assuming that the finite collection of  $f$ 's image  $f(X_1), \dots, f(X_n)$  is multivariate normal with mean vector  $\mathbf{m}$  and covariance matrix  $\mathbf{K}$ . This can be denoted as

$$f(X_t) \sim \mathcal{GP}(m(X_t), K(X_t, X_s)),$$

where  $m(X_t)$  is the mean of  $f$  evaluated at  $X_t$  and  $K(X_t, X_s)$  is the covariance of  $f$  evaluated at  $X_t$  and  $X_s$ . Gaussian process regression, from  $X \in \mathcal{X}$  to  $Y \in \mathcal{Y}$ , with Gaussian error is defined by the following model

$$\begin{aligned} Y_t &= f(X_t) + \epsilon, \\ (1) \quad f(X_t) &\sim \mathcal{GP}(m(X_t), K(X_t, X_s)), \\ \epsilon &\sim N(0, \sigma^2). \end{aligned}$$

Gaussian process regression is nonparametric because we place a prior distribution on the function  $f$  directly, rather than finitely parameterizing it. Also, because we assume  $\epsilon$  is Gaussian and  $f \sim \mathcal{GP}(m(X), K(X, X'))$ , the posterior of  $f$  is still a Gaussian process by conjugacy of the multivariate normal distribution. Moreover, we can analytically compute the

posterior predictive distribution of  $f(X_m)$ , based on  $X_m$  and the training data  $D$ , as

$$(2) \quad \begin{aligned} P(f(X_m) | X_m, D) &= N(\mu_m, K_m), \\ \mu_m &= m(X_m) + K(X_m, \mathbf{X})(K(\mathbf{X}, \mathbf{X}) + \sigma^2 \mathbf{I}_n)^{-1} \mathbf{Y}, \\ K_m &= K(X_m, X_m) - K(X_m, \mathbf{X})(K(\mathbf{X}, \mathbf{X}) + \sigma^2 \mathbf{I}_n)^{-1} K(\mathbf{X}, X_m), \end{aligned}$$

where  $\mathbf{Y}$  denotes the  $n \times 1$  vector with entries  $Y_i$  for  $i \in 1, \dots, n$  and  $\mathbf{X}$  denotes the  $n \times q$  matrix with rows  $X_i$  for  $i \in 1, \dots, n$ . We denote  $K(X_m, \mathbf{X})$  as the  $1 \times n$  vector with entries  $K(X_m, X_j)$  for  $j \in 1, \dots, n$  and  $K(\mathbf{X}, \mathbf{X})$  as the  $n \times n$  matrix with entries  $K(X_i, X_j)$  for  $i, j \in 1, \dots, n$ . The vector  $K(\mathbf{X}, X_m)$  is transpose of  $K(X_m, \mathbf{X})$  and  $\mathbf{I}_n$  is the  $n \times n$  identity matrix. Thus, given the prior mean and covariance functions, and historical data, we can automatically compute the posterior predictive distribution of  $f$  at any test point  $X_m$ . Consequently, the posterior prediction distribution of  $Y_m$  is  $P(Y_m | X_m, D) = N(\mu_m, K_m + \sigma^2)$ .

**2.2. Deep neural network kernels.** The mean function,  $m(X_t)$ , can often be set to a constant, such as 0, for stationary processes or to some (non)linear trend over  $\mathcal{X}$ . The covariance function,  $K(X_t, X_s)$ , is typically more difficult to specify, particularly for complex objects like climate model output where  $X_t, X_s$  are ensembles of climate fields. Some recent works have defined complex covariance functions through low rank approximations (Katzfuss, 2017) or dimension augmentation (Bornn, Shaddick and Zidek, 2012; Shand and Li, 2017). While these approaches provide general covariance functions for GPR, they may be difficult to justify or compute for our particular problem of mapping ensembles of climate models to reanalysis fields.

In Lee et al. (2017), the authors showed that deep Bayesian neural networks (MacKay, 1992; Neal, 2012; Wilson and Izmailov, 2020) define valid, typically non-stationary, covariance functions. They showed that untrained, infinitely wide, Bayesian neural networks (BNN) are equivalent to Gaussian processes with a recursively defined covariance function. This family of Gaussian processes is termed Neural Network Gaussian Processes (NNGP).

We review the general form of the NNGP covariance function and present a special case based on ReLU activations that we use in our study. Let  $\Phi_A$ , denote an untrained, fully connected deep neural network with architecture  $A$ , and mapping from  $\mathcal{X}$  to  $\mathcal{Y}$ . We denote the  $i$ 'th output of the  $l$ 'th layer of  $\Phi_A$  given input  $X_t \in \mathcal{X}$  as

$$(3) \quad Z_i^l(X_t) = b_i^l + \sum_{j=1}^{N_l} W_{ij}^l X_j^l(X_t), \quad X_j^l(X_t) = \phi(Z_j^{l-1}(X_t)),$$

where  $\phi$  is an activation function, such as ReLU or Tanh (Goodfellow, Bengio and Courville, 2016), and  $N_l$  is the layer width. We further assume that the weights ( $W_{ij}^l$ ) and biases ( $b_i^l$ ) of  $\Phi_A$  follow symmetric, zero mean prior distributions with prior variances  $\text{Var}(W_{ij}) = \sigma_w^2/N_l$  and  $\text{Var}(b_i) = \sigma_b^2$ .

By letting  $N_l \rightarrow \infty$ ,  $Z_i^l(X)$  will converge to a Gaussian distribution with mean zero and covariance

$$(4) \quad K^l(X_t, X_s) = \sigma_b^2 + \sigma_w^2 \mathbb{E}_{Z_i^{l-1}}[\phi(Z_i^{l-1}(X_t))\phi(Z_i^{l-1}(X_s))],$$

by the central limit theorem (Lee et al., 2017; Garriga-Alonso, Rasmussen and Aitchison, 2018). Here  $\mathbb{E}[\cdot]$  denotes the expected value operator. Lee et al. (2017) further defines the deterministic function  $F_\phi$  as

$$(5) \quad F_\phi(K^l(X_t, X_t), K^l(X_t, X_s), K^l(X_s, X_s)) = \mathbb{E}_{Z_i^{l-1}}[\phi(z_i^l(X_t))\phi(z_i^l(X_s))].$$

Assuming  $\Phi_A$  has  $L$  layers, we can write the output covariance  $K^L(X_t, X_s)$  as a sequence of non-linear transformations

$$\begin{aligned}
 K^L(X_t, X_s) &= \sigma_b^2 + \sigma_w^2 F_\phi(K^{L-1}(X_t, X_t), K^{L-1}(X_t, X_s), K^{L-1}(X_s, X_s)) \\
 &\vdots \\
 K^1(X_t, X_s) &= \sigma_b^2 + \sigma_w^2 F_\phi(K^0(X_t, X_t), K^0(X_t, X_s), K^0(X_s, X_s)) \\
 K^0(X_t, X_s) &= \sigma_b^2 + \sigma_w^2 (X_t^T X_s / d_{\text{in}}),
 \end{aligned}
 \tag{6}$$

which reveals a recursive structure since each layer has a covariance function based on Equation 4. Here  $d_{\text{in}}$  denotes the dimension of the inputs, i.e. the total number of grid points across all models in the ensemble. In many cases  $F_\phi(K^l(X_t, X_t), K^l(X_t, X_s), K^l(X_s, X_s))$  can be computed analytically for each  $l \in 1, \dots, L$ . For example, if  $\phi$  is a ReLU activation, then

$$\begin{aligned}
 F_\phi(K^l(X_t, X_t), K^l(X_t, X_s), K^l(X_s, X_s)) \\
 &= \frac{1}{2\pi} \sqrt{K^l(X_t, X_t) K^l(X_s, X_s)} \left( \sin(\theta_{X_t, X_s}^l) + (\theta_{X_t, X_s}^l - \pi) \cos(\theta_{X_t, X_s}^l) \right) \\
 \theta_{X_t, X_s}^l &= \arccos \left( \frac{K^l(X_t, X_s)}{\sqrt{K^l(X_t, X_t) K^l(X_s, X_s)}} \right).
 \end{aligned}$$

With  $K^L(X_t, X_s)$ , we can define a GPR that exactly mimics the predictions of an infinitely wide neural network  $\Phi_A$ . That is, if we had the posterior distribution of all weights and biases,  $\Phi_A$  would make identical predictions to GPR with the  $K^L(X_t, X_s)$  kernel. For finite width networks, GPR will only approximate the predictions. However, GPR can quantify its predictive uncertainty naturally since it yields entire posterior distributions. GPR also requires substantially fewer observations to train since we need only to optimize three parameters  $\sigma_b^2$ ,  $\sigma_w^2$  and  $\sigma^2$  rather than several million, as is common in deep learning.

**3. Model.** We denote our training dataset as the sequence  $D = \{(X_t, Y_t)\}_{t=1}^n$ . Each  $X_t$  represents a *ensemble* of  $m$  gridded climate model fields, all observed at time  $t$ , and each  $Y_t$  represents the gridded reanalysis field at time  $t$ . We represent each  $X_t$  as a vector by vectorizing each of the  $m$  fields at time  $t$  and concatenating the resulting vectors into a single vector. We also represent each  $Y_t$  as a vector of length  $d = n_{\text{lat}} \times n_{\text{lon}}$ , where  $n_{\text{lat}}$  and  $n_{\text{lon}}$  denote the number of latitude and longitude grid points, respectively.

Denote  $Y_t(p)$  as value of  $Y_t$  at location  $p$ , where  $1 \leq p \leq d$ . We model  $Y_t(p)$  as

$$\begin{aligned}
 Y_t(p) &= \beta^T \bar{X}_t + f(X_t, p) + \epsilon, \\
 f(X_t, p) &\sim \mathcal{GP}(0, K_\theta(X_t, X_s)), \\
 \epsilon &\sim N(0, \sigma^2).
 \end{aligned}
 \tag{7}$$

The key simplifying assumption is that each spatial location in  $Y_t$  has the same prior distribution, meaning parameters can be shared across all locations.

*Data level* — The first term,  $\beta^T \bar{X}_t$ , is a linear combination of the climate model means at time  $t$ ,  $\bar{X}_t = (\bar{X}_{t,1}, \dots, \bar{X}_{t,m})$ . The coefficients  $\beta = (\beta_1, \dots, \beta_m)$  are estimated with simple linear regression of  $\bar{X}_t$  against the reanalysis means  $\bar{Y}_t$ . The term  $\beta^T \bar{X}_t$  is intended to keep the predictions of  $f(X_t, p)$  relatively calibrated towards the ensemble spatial mean. The second term,  $f(X_t, p)$ , is the  $p$ 'th output of the unknown function  $f$  applied to the model ensemble  $X_t$ . The function  $f$  is how we transform model ensembles into reanalysis fields after accounting for the trend. This term is nonparametric because we place a prior directly



on  $f$ , rather than parameterizing it. Finally,  $\epsilon$  represents the residual noise after accounting for the trend  $\beta^T \bar{X}_t(p)$  and the neural network prediction  $f(X_t, p)$ .

*Prior level* — Both prior distributions have zero mean to ensure all prior mean behavior is contained in the trend term  $\beta^T \bar{X}_t(p)$ . The overall prior covariance, however, is defined by two terms: the NNGP covariance  $K_\theta$  with parameters  $\theta = \{\sigma_w^2, \sigma_b^2\}$  (Section 2) and the noise variance  $\sigma^2$ . The NNGP covariance  $K_\theta$  computes the covariance between  $X_t, X_s$  for all  $t, s \in 1, \dots, n$ . The residual variance,  $\sigma^2$ , is constant based on the assumption that  $f$  captures all heterogenous spatial variability.

*Parameters* — Rather than placing hyperpriors on the unknown parameters  $\beta$ ,  $\sigma^2$  and  $\theta$ , we estimate them by following the common approach for Gaussian process regression (Rasmussen and Williams, 2006). We discuss our parameter estimation strategy in Section A of the appendix. In addition to these obvious parameters, there are also several hidden parameters not appearing in Equation 7, which cannot be optimized directly. These parameters define the architecture  $A$  of the underlying neural network  $\Phi_A$ , which ultimately defines  $K_\theta$ .

For simplicity, we assume fully connected layers with ReLU activations since this yields an analytical form for  $K_\theta$ . This simple architecture performed well in the experiments, so more complex layer types like convolutional layers were unnecessary. For the depth  $L$ , we found that predictive performance is relatively insensitive to  $L$  for  $3 \leq L \leq 30$ , with  $L = 10$  serving as a compromise between accuracy and runtime. For all experiments (Section 4) and reanalysis results (Section 5), we use  $L = 10$ .

*Prediction* — Given a new multi-model ensemble, say  $X_m$  for  $m > n$ , we can integrate  $X_m$  into a probabilistic forecast by computing the posterior prediction distribution of the unobserved reanalysis field  $Y_m$ . Let  $Y_m(p)$  denote  $Y_m$  at the location  $p$ , for all  $1 \leq p \leq d$ , and let  $\mathbf{Y}(p)$  denote the  $n \times 1$  vector  $[Y_1(p), \dots, Y_n(p)]$ . Then the posterior predictive distribution (Section 2.2) of  $Y_m(p)$  is given by

$$\begin{aligned} P(Y_m(p) | X_m, D) &= N(\mu_m(p), K_m(p)) + N(0, \sigma^2), \\ \mu_m(p) &= \beta^T \bar{X}_m + K_\theta(X_m, \mathbf{X})(K_\theta(\mathbf{X}, \mathbf{X}) + \sigma^2 \mathbf{I}_n)^{-1} \mathbf{Y}(p), \\ K_m(p) &= K_\theta(X_m, X_m) - K_\theta(X_m, \mathbf{X})(K_\theta(\mathbf{X}, \mathbf{X}) + \sigma^2 \mathbf{I}_n)^{-1} K_\theta(\mathbf{X}, X_m). \end{aligned}$$

Here we have again used the notation that  $K_\theta(X_m, \mathbf{X})$  is an  $1 \times n$  vector with entries  $K_\theta(X_m, X_j)$  for  $j \in 1, \dots, n$  and  $K_\theta(\mathbf{X}, \mathbf{X})$  is an  $n \times n$  matrix with entries  $K_\theta(X_i, X_j)$  for  $i, j \in 1, \dots, n$ . Note that  $K_m(p)$  is the same for all  $p$  since it is based entirely on the covariance parameters  $\sigma^2, \sigma_b^2$ , and  $\sigma_w^2$  which are identical at all locations. We predict the field  $Y_m$  pointwise as  $\hat{Y}_m(p) = \mu_m(p)$  and quantify uncertainty pointwise with  $K_m(p) + \sigma^2$  for all  $p \in 1, \dots, d$ .

**4. Numerical experiments in model prediction.** We compare our model, NN-GPR, against baseline methods: ensemble averaging (EA), weighted ensemble averaging (WEA) (Knutti et al., 2017), and ensemble regression (LM) (Bracegirdle and Stephenson, 2012). For ensemble regression, we pointwise regress the (resized) climate models in the ensemble onto the target field. We exclude hierarchical Bayesian methods (Sansom, Stephenson and Bracegirdle, 2017) from comparison due to their complexity, computational cost, and lack of software implementation for our problem.

We use a “perfect model” test to compare integration methods, whereby one model is held out from an ensemble, and the remainder of the ensemble is used to predict the held out model (Knutti et al., 2017). We consider a small 16 member ensemble of monthly average 2-meter surface temperature (T2M) fields and average total precipitation (PR) fields. This ensemble includes ACCESS-CM2, BCC-CSM2-MR, CMCC-CM2-SR5, CanESM5-CanOE,

two ensemble runs of CanESM5, FIO-ESM-2-0, GFDL-ESM4, INM-CM5-0, two ensemble runs of IPSL-CM6A-LR, KACE-1-0-G, MCM-UA-1-0, and two ensemble runs of MIROC-ES2L (Eyring et al., 2016).

For each model, we have gridded T2M and PR monthly averages. Each model is observed on either a 100, 250, or 500km grid, depending on the model. We run 16 perfect model tests, in which each model from the ensemble is held out and predicted by the remaining 15 models. In each test, we train each method on historical model runs from 1950-2015 and SSP245 forced runs from 2015-2020. We evaluate each method’s predictive performance on SSP245 forced runs from 2021-2100 and divide the test set into eight decadal blocks, 2021-2030, 2031-2040, . . . , 2091-2100, to measure relative performance over time.

**4.1. Climate field prediction.** We quantify predictive accuracy with the mean squared error (MSE) and the Structural Similarity Index Measure (SSIM) (Wang and Bovik, 2002). MSE quantifies overall accuracy, and SSIM quantifies the visual similarity of the prediction with the target. SSIM overcomes a shortcoming of MSE: a low MSE is achievable even with predictions that do not resemble the target. High SSIM values indicate that structural features of the climate model, such as high precipitation events and orographic temperature gradients (Figure 1), are well preserved. Moreover, high SSIM means the predictions are not blurred, noisy, skewed, or otherwise distorted, even at very fine scales. We use the standard equal area-weighted MSE

$$MSE(y, \hat{y}) = \frac{1}{n} \sum_p w_p (y - \hat{y})^2,$$

where  $w_p$  are latitude based weights (North et al., 1982),  $y$  is the observation and  $\hat{y}$  is the prediction. For SSIM we use the standard, though complex, sliding window SSIM described in Wang and Bovik (2002).

Table 1 shows the average (over the 16 perfect model tests) of the MSE and SSIM scores for each method applied to temperature and precipitation prediction. NN-GPR improves over existing approaches in the first five decades (2020-2070) but deteriorates to similar performance as the regression model in the last three decades (2070-2100). NN-GPR is particularly effective in the first three decades (2020-2050). EA and WEA have consistently much higher MSE (1.5-3x) and lower SSIM values over the whole prediction period. Lower MSE values indicate that NN-GPR more accurately reproduces the individual model simulations. Higher SSIM scores indicate NN-GPR’s predictions are sharper, less blurry, and less distorted from the truth than existing methods.

In the far future (2070-2100), however, NN-GPR’s predictive performance for temperature begins to decline. The reason is because of the way NN-GPR manages bias and variance (Figure 2). NN-GPR shows low bias over the entire prediction interval, but the variance trends upwards. Over longer time horizons (2050-2100 shaded in grey), the variance steadily increases, leading to inflated MSE values. However, the bias remains stable around zero. Thus, while the NN-GPR may produce marginally suboptimal predictions in the long term (2080 - 2100), we expect the spatial averages of those predictions, such as global mean surface temperatures, to be relatively unbiased.

The variance trends upwards because the SSP245 models (inputs) become more and more unlike the training (historical) models in the future. That is, our T2M predictions suffer from unmitigated *covariate shift* (Shimodaira, 2000) (Figure 3a). NN-GPR predictions based on inputs (climate models) that are increasingly dissimilar from the training data converge to the same weighted average of the training reanalysis fields plus the trend. After further analysis, we found that this resulted in over smoothing of the distinctive features of each reanalysis field. Thus, the prediction error variance, along with SSIM, increased, but the bias remained

Average 2M Surface Temperature – T2M

| Decade    | MSE ( $\downarrow$ ) |       |       |       | SSIM ( $\uparrow$ ) |       |       |       |
|-----------|----------------------|-------|-------|-------|---------------------|-------|-------|-------|
|           | NN-GPR               | LM    | WEA   | EA    | NN-GPR              | LM    | WEA   | EA    |
| 2021–2030 | 0.663                | 0.799 | 1.234 | 2.100 | 0.928               | 0.916 | 0.892 | 0.842 |
| 2031–2040 | 0.690                | 0.802 | 1.235 | 2.082 | 0.926               | 0.915 | 0.892 | 0.842 |
| 2041–2050 | 0.732                | 0.825 | 1.275 | 2.110 | 0.920               | 0.912 | 0.888 | 0.839 |
| 2051–2060 | 0.798                | 0.881 | 1.33  | 2.147 | 0.914               | 0.907 | 0.884 | 0.836 |
| 2061–2070 | 0.844                | 0.897 | 1.341 | 2.152 | 0.909               | 0.904 | 0.884 | 0.837 |
| 2071–2080 | 0.891                | 0.906 | 1.357 | 2.158 | 0.902               | 0.903 | 0.882 | 0.834 |
| 2081–2090 | 0.949                | 0.927 | 1.371 | 2.147 | 0.896               | 0.900 | 0.880 | 0.834 |
| 2091–2100 | 1.002                | 0.956 | 1.393 | 2.161 | 0.891               | 0.897 | 0.878 | 0.832 |

Average Total Precipitation – PR

| Decade    | MSE ( $\downarrow$ ) |       |       |       | SSIM ( $\uparrow$ ) |       |       |       |
|-----------|----------------------|-------|-------|-------|---------------------|-------|-------|-------|
|           | NN-GPR               | LM    | WEA   | EA    | NN-GPR              | LM    | WEA   | EA    |
| 2021–2030 | 2.249                | 2.587 | 2.92  | 3.454 | 0.642               | 0.608 | 0.562 | 0.542 |
| 2031–2040 | 2.328                | 2.688 | 3.023 | 3.569 | 0.638               | 0.604 | 0.56  | 0.54  |
| 2041–2050 | 2.372                | 2.721 | 3.066 | 3.626 | 0.634               | 0.603 | 0.559 | 0.539 |
| 2051–2060 | 2.512                | 2.845 | 3.195 | 3.744 | 0.628               | 0.599 | 0.555 | 0.536 |
| 2061–2070 | 2.623                | 2.936 | 3.284 | 3.835 | 0.622               | 0.597 | 0.554 | 0.535 |
| 2071–2080 | 2.692                | 2.986 | 3.323 | 3.891 | 0.617               | 0.595 | 0.552 | 0.533 |
| 2081–2090 | 2.748                | 3.035 | 3.389 | 3.965 | 0.615               | 0.593 | 0.55  | 0.531 |
| 2091–2100 | 2.839                | 3.113 | 3.443 | 4.004 | 0.61                | 0.591 | 0.55  | 0.531 |

TABLE I

**Top:** Average MSE and SSIM for four model integration approaches applied to **surface temperature** field prediction, broken out by the 8 decades in the testing period. NN-GPR is our method, LM is pointwise linear regression, WEA is a reliability weighted ensemble average, and EA is the naive ensemble average. **Bottom:** Average MSE and SSIM for the same model integration approaches applied to **total precipitation** field prediction, broken out by the 8 decades in the testing period. Arrows indicate whether higher ( $\uparrow$ ) or lower ( $\downarrow$ ) numbers are better.

low. T2M shows strong evidence of covariate shift due to the mismatch between the train and test point clouds and thus higher variance inflation over time.

PR, however, does not experience the same degree of performance deterioration that T2M does since PR does not experience the same covariate shift as T2M (Figure 3b). We expect a substantial covariate shift in T2M due to climate change, but the shift for precipitation is more slight when looking at monthly averages. Thus, total monthly precipitation fields under SSP245 in the far future are similar to the training data, so variance and SSIM do not necessarily inflate and deflate, respectively.

These results indicate that NN-GPR can approximate individual model simulations and even improve over highly parameterized models such as pointwise linear regression. Thus NN-GPR can be a highly effective approach to climate model integration. However, its superior prediction skill is tied to our ability to mitigate covariate shift, such as by including an explicit trend term. Figure 3 showed that this shift is not an inherent feature of time but the variable type. Thus, any climate model integration needs to consider, on a case-by-case basis, how to quantify and account for covariate shift, i.e., simulated climate change.

**4.2. Uncertainty quantification.** We compare each method’s uncertainty quantification (UQ) abilities through two metrics. The first is the Continuous Ranked Probability Score (CRPS), which is commonly used to assess probabilistic predictions in climate science (Gneiting and Raftery, 2007). The second is the empirical coverage of the target process



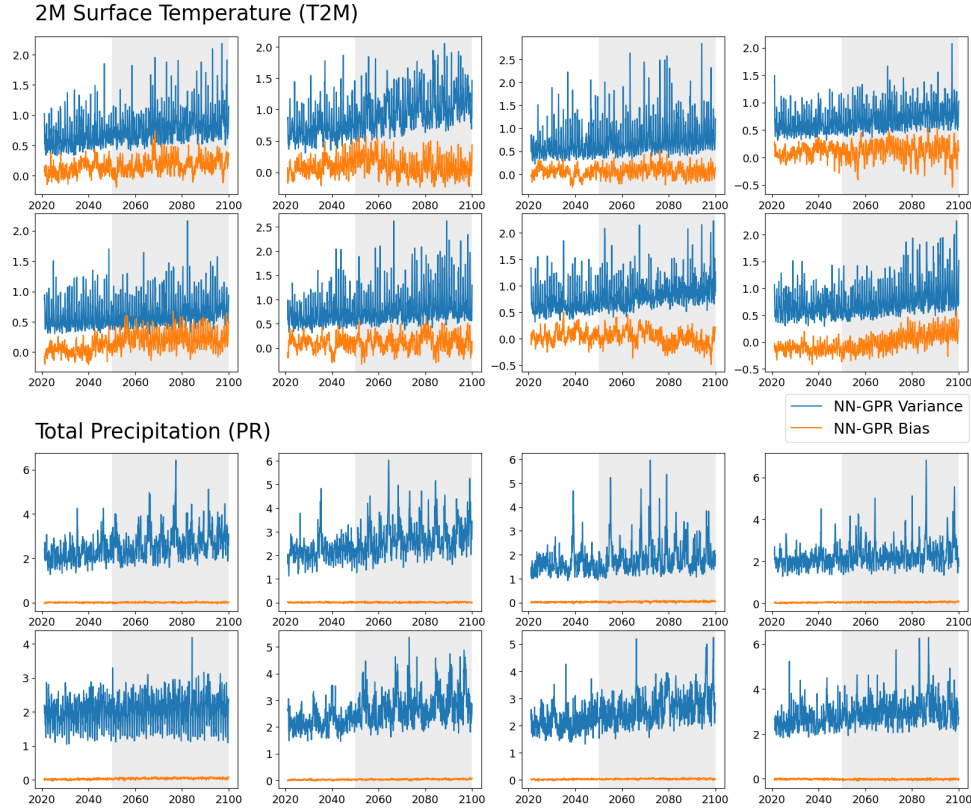


FIG 2. Bias-variance decomposition of NN-GPR's prediction MSE for 8 of the 16 models in the ensemble for T2M (top) and PR (bottom). All predictions are made on the test set using SSP245 forced model simulations, as in Table 1.

by each model's prediction intervals. As a Bayesian method, NN-GPR produces credible intervals rather than confidence intervals, so nominal coverage is not guaranteed, although it is often observed.

Table 2 shows that NN-GPR has slightly higher CRPS scores than LM, though significantly lower CRPS scores than EA for 2-meter surface temperature prediction (T2M). For precipitation, the rankings are the same, although the three methods are much more competitive with each other. NN-GPR shows conservative coverage on T2M, maintaining around 98% coverage (on T2M) and 95% coverage (on PR) versus the nominal 0.95 level. While the T2M coverage is slightly higher than desired, we do not underestimate the variability as the LM method does past 2050. These results indicate that our approach often produces slightly wide prediction intervals, leading to an inflated CRPS and over-coverage.

To see why and where over-coverage is occurring, we created average CRPS maps for NN-GPR and LM by averaging their raw CRPS scores in time rather than in time and space as was done to create Table 2. We then subtracted NN-GPR's CRPS maps from LM's CRPS maps to produce Figure 4a. This panel shows the map of the differences by averaging over the entire prediction period.

For the T2M predictions, NN-GPR tends to have lower CRPS scores over land, particularly in the northern hemisphere, while LM shows lower CRPS scores over the ocean. A clear pattern emerges near the equator for the TP predictions where NN-GPR again significantly improves in CRPS over LM. To see why these patterns emerge in both variables, we created a second set of maps in (Figure 4b, 4d). These panels show locations where NN-GPR has lower

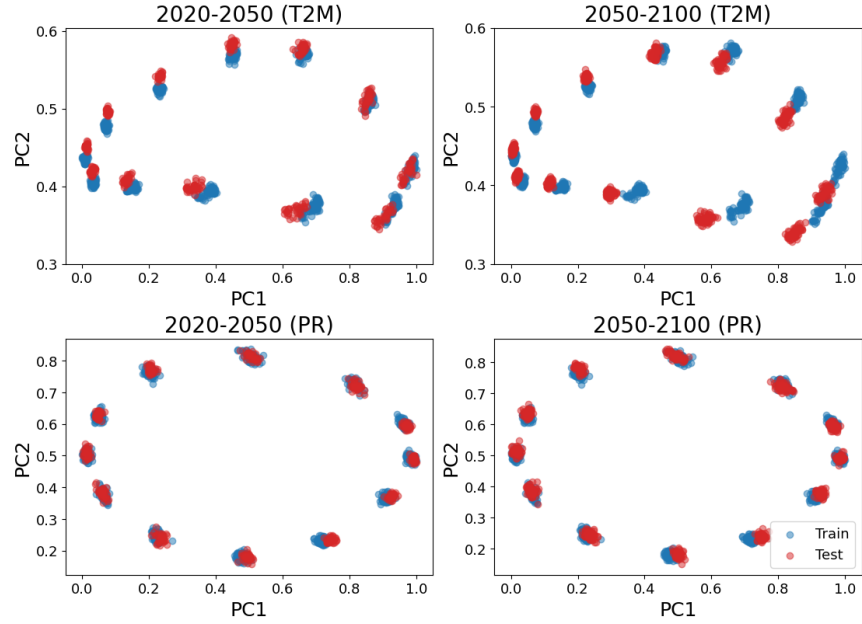


FIG 3. Projections of the historical climate model data and the future SSP model simulations onto the top two principal components of the historical model data. Model means and variances were removed before projection. The top row shows projections of T2M data, and the bottom row shows PR data, divided into the near term (2020-2050) and long term (2050-2100) sections of the prediction period.

Average 2M Surface Temperature –T2M

| Decade    | CRPS ( $\downarrow$ ) |       |       |       | Coverage (0.95) |       |       |       |
|-----------|-----------------------|-------|-------|-------|-----------------|-------|-------|-------|
|           | NN-GPR                | LM    | WEA   | EA    | NN-GPR          | LM    | WEA   | EA    |
| 2021–2030 | 0.46                  | 0.428 | 0.458 | 0.727 | 0.98            | 0.955 | 0.989 | 0.942 |
| 2031–2040 | 0.469                 | 0.431 | 0.456 | 0.724 | 0.98            | 0.953 | 0.988 | 0.942 |
| 2041–2050 | 0.484                 | 0.438 | 0.462 | 0.732 | 0.98            | 0.951 | 0.989 | 0.943 |
| 2051–2060 | 0.504                 | 0.457 | 0.467 | 0.741 | 0.98            | 0.940 | 0.988 | 0.943 |
| 2061–2070 | 0.518                 | 0.465 | 0.469 | 0.744 | 0.98            | 0.934 | 0.988 | 0.944 |
| 2071–2080 | 0.533                 | 0.468 | 0.469 | 0.745 | 0.98            | 0.933 | 0.987 | 0.944 |
| 2081–2090 | 0.550                 | 0.476 | 0.469 | 0.745 | 0.98            | 0.928 | 0.987 | 0.944 |
| 2091–2100 | 0.565                 | 0.486 | 0.471 | 0.748 | 0.98            | 0.922 | 0.986 | 0.944 |

Average Total Precipitation – PR

| Decade    | CRPS ( $\downarrow$ ) |       |       |       | Coverage (0.95) |       |       |       |
|-----------|-----------------------|-------|-------|-------|-----------------|-------|-------|-------|
|           | NN-GPR                | LM    | WEA   | EA    | NN-GPR          | LM    | WEA   | EA    |
| 2021–2030 | 0.58                  | 0.563 | 0.399 | 0.633 | 0.953           | 0.961 | 0.95  | 0.942 |
| 2031–2040 | 0.588                 | 0.572 | 0.404 | 0.641 | 0.953           | 0.959 | 0.95  | 0.942 |
| 2041–2050 | 0.593                 | 0.575 | 0.407 | 0.645 | 0.953           | 0.958 | 0.95  | 0.942 |
| 2051–2060 | 0.608                 | 0.587 | 0.413 | 0.654 | 0.951           | 0.956 | 0.95  | 0.942 |
| 2061–2070 | 0.618                 | 0.593 | 0.415 | 0.659 | 0.951           | 0.955 | 0.949 | 0.942 |
| 2071–2080 | 0.626                 | 0.599 | 0.419 | 0.664 | 0.950           | 0.953 | 0.949 | 0.942 |
| 2081–2090 | 0.632                 | 0.603 | 0.422 | 0.669 | 0.949           | 0.952 | 0.949 | 0.942 |
| 2091–2100 | 0.640                 | 0.609 | 0.424 | 0.672 | 0.949           | 0.951 | 0.949 | 0.942 |

TABLE 2

**Top:** Average CRPS and prediction interval coverage for the four different model integration approaches on T2M, broken out by the 8 decades in the testing period. **Bottom:** Same summary measures as the top for each model applied to precipitation. Arrows indicate whether higher ( $\uparrow$ ) or lower ( $\downarrow$ ) numbers are better.

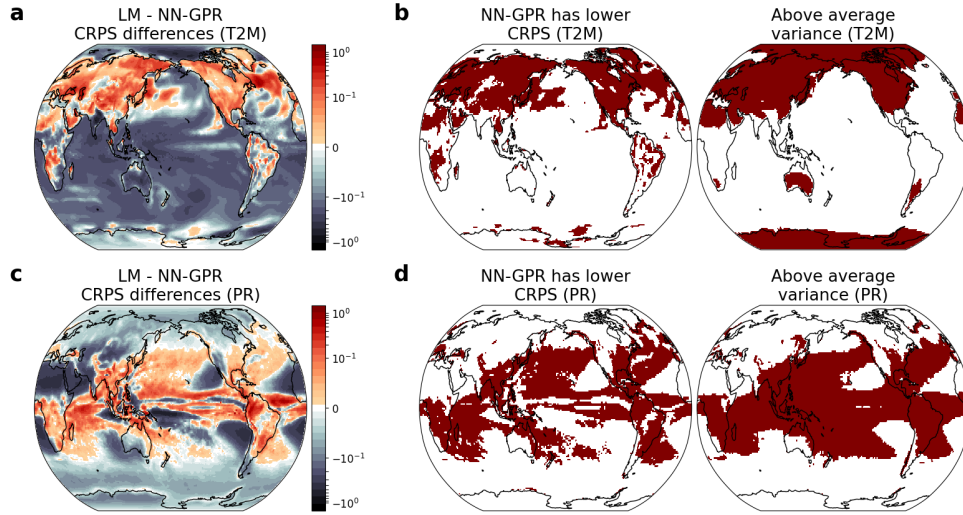


FIG 4. Panel (a) and (c) – Average difference in CRPS scores (LM - NN-GPR) for a single example climate model (ACCESS-CM2). Orange regions indicate NN-GPR had lower CRPS than LM, while blue-grey indicates NN-GPR had higher CRPS than LM. Panel (b) and (d) – The leftmost plots show a binarized version of panels (a) and (c) to highlight the exact regions where NN-GPR has lower CRPS scores than LM. The rightmost plots show regions in the ACCESS-CM2 output where the variance was higher than average

CRPS than LM (improvements) and locations where the reanalysis fields exhibit higher than average variance. Figures 4b and 4d indicate NN-GPR represents the reanalysis distribution better in regions of high variability. In areas of low variability, NN-GPR tends to overestimate the prediction intervals, which leads to high CRPS and high coverage.

Combining the results from Table 1 with the maps in Figure 4, we conclude that NN-GPR is more accurate than existing methods. However, its prediction intervals are often slightly too wide, i.e., under-confident. Wide prediction intervals lead to the higher CRPS and empirical coverage scores seen in Table 2. However, we also observed that NN-GPR tends to represent variability in high variance regions better than the other methods (Figure 4). This means optimizing the variance term in NN-GPR favors representing high variance regions at the cost of being under-confident in low variance regions since all regions are constrained to share a single variance value.

**5. Global and regional projections under SSP245.** Global climate models are essential tools for understanding how Earth’s climate changes and for projecting regional impacts. Data products, such as the Coupled Model Intercomparison Project (CMIP6) (Eyring et al., 2016), exist explicitly to study the projections from different climate models under a wide range of external forcings and socio-economic scenarios. Two of the most widely studied variables are temperature and precipitation. There is broad agreement between climate models that global temperatures are rising and that precipitation will become more intense and less frequent in the future (Trenberth, 2011; Giorgi, Raffaele and Coppola, 2019). However, the models can disagree significantly on how that process unfolds in time and space.

We now use NN-GPR to project future surface temperature and precipitation under Shared Socioeconomic Pathway 2 using RCP 4.5 (SSP245) (O’Neill et al., 2016). We use the CMIP6 climate models as input to our GPR and target reanalysis fields in this application. Reanalysis data comes from the ERA5 reanalysis product (Hersbach et al., 2020) and spans 1950-2021. We use NN-GPR to separately predict the 2-Meter Surface Temperature fields (T2M) and the Total Precipitation fields (PR) on single pressure levels, based on the 16 member CMIP6

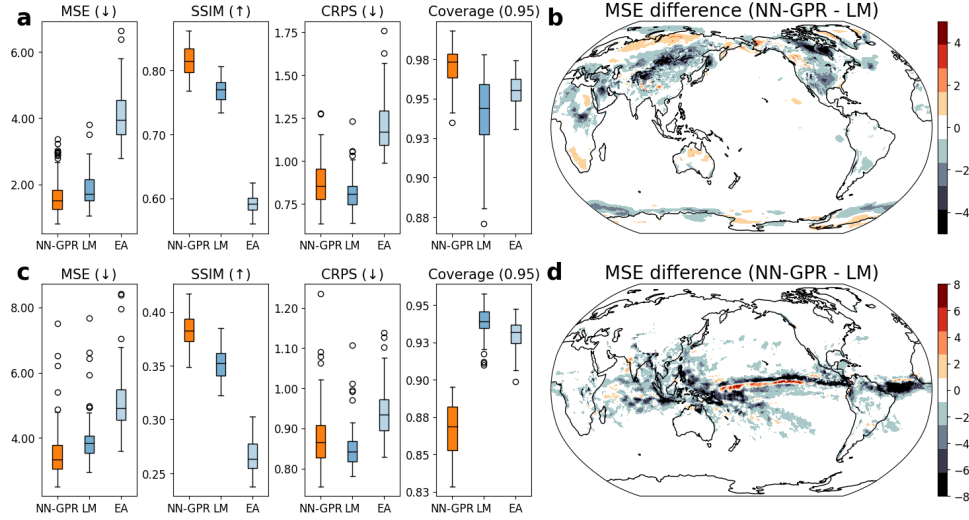


FIG 5. Boxplots for T2M (a) and PR (c) comparing the accuracy and UQ measures for each method on the reanalysis test data (2015-2021). Arrows indicate whether higher (↑) or lower (↓) numbers are better. Panels (b) and (d) show spatial differences in the MSE (averaged over time) of NN-GPR and LM for T2M(b) and PR(d).

ensembles of T2M and PR. Because there is no ground truth after 2021, we compare our results against the traditional ensemble average predictions (EA) and the pointwise linear model (LM). Computing the weighted ensemble average (WEA) proved too computational prohibitive on the reanalysis data.

**5.1. Global climate projections.** We use the proposed NN-GPR method, LM, and EA to produce high-resolution projections under SSP245 from 2015 through 2100. We focus on the differences between NN-GPR and LM since these were the two most competitive approaches in Section 4.1. We first test the performance of the two approaches by comparing their predictions on a small out of sample period (2015-2021) using the same metrics in Section 4 (Figure 5).

Figures 5a, 5b shows the MSE, SSIM, CRPS, and empirical coverage of our proposed NN-GPR method against LM and EA on temperature (T2M) and precipitation (PR) over the test period. The results are consistent with the experiments (Section 4, Tables 1 and 2), with NN-GPR showing improved average prediction metrics (MSE: 1.69, SSIM: 0.82) compared to LM (MSE: 1.88, SSIM: 0.77) and EA (MSE: 4.07, SSIM: 0.59). Therefore, NN-GPR more accurately predicts the held-out historical observations and produces sharper, less distorted predictions. LM tends to have better uncertainty quantification metrics (CRPS: 0.82, Coverage: 0.94) than NN-GPR (CRPS: 0.88, Coverage: 0.97) since LM uses a spatially varying variance.

The relative MSE maps in Figures 5b and 5d illustrate where NN-GPR has higher historical skill than LM by showing regions where NN-GPR has a lower squared error. Overall, most locations have comparable MSE, although NN-GPR again improves in regions of high variability as in Figure 4. For T2M, these include high latitude landmasses such as North America and Northern Asia. Improvements in PR largely stem from improvements in the Intertropical Convergence Zone (ITCZ) and southeast Asia (SEA). These findings are consistent with the numerical results in (Section 4, Figure 4).

Figure 5 supports our assumption that predictive skill on climate models (Section 4) broadly translates to predictive skill on historical observation data, which can help reduce future projection uncertainty. To see how each method’s projections differ, we first compare

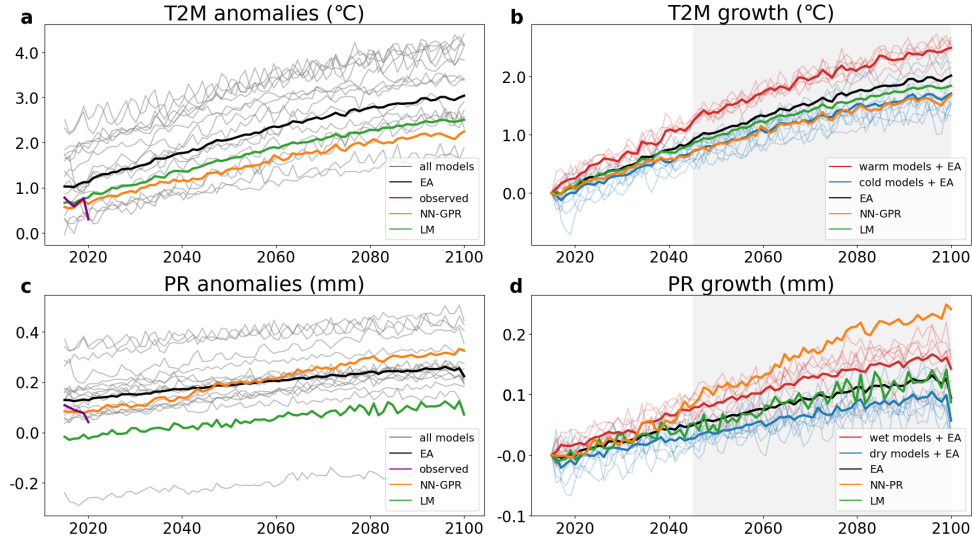


FIG 6. Panels (a) and (c) show yearly T2M and PR averages of each method, individual climate model averages (all models), and the observations. Panels (b) and (d) show projected T2M and PR growth of each method starting from 2015. In panel (b), a “warm” model has T2M growth over  $1^{\circ}\text{C}$  by 2045 and in panel (d) a “wet” model has PR growth over  $0.05\text{mm}$  by 2045.

the yearly global averages (T2M and PR) as estimated by each method (Figure 6). NN-GPR and LM both run cool compared to the model average ( $0.67^{\circ}\text{C}$  and  $0.44^{\circ}\text{C}$  below EA on average, respectively, in Figure 6a), though still within the model spread. NN-GPR produces similar global precipitation levels as EA ( $0.01\text{mm}$  higher than EA on average). At the same time, LM shows a considerably drier climate ( $0.15\text{mm}$  lower than EA on average) than all but a single ensemble member (Figure 6c). Figures 6a and 6c show that NN-GPR does not fundamentally alter the global averages beyond a slight shift and slope change to better fit the observed averages.

The effect of NN-GPR is seen at smaller scales (Figure 5), yet it has a profound impact on overall global patterns (Figures 6b and 6d). The T2M plot in figure 6b shows that there are two groups of models in the data, with six of the models projecting rapid surface temperature increases around 2040, while the remaining ten steadily increase. NN-GPR closely tracks these cooler, steadier models and disregards the rapidly warming models, resulting in projected warming of  $1.68^{\circ}\text{C}$  from 2020 to 2100 compared to  $2.01^{\circ}\text{C}$  shown by the EA. Around 2045-2050, NN-GPR also begins projecting PR growth uncharacteristic of any ensemble model. This suggests that NN-GPR can produce long-range dynamics different from the climate model inputs.

Figure 7 shows the spatial differences between NN-GPR’s projections and LMs and EA’s projections to reveal why NN-GPR projects a relatively cooler and wetter future than either LM or EA. Panel 7a shows that T2M differences are primarily driven by the Pacific ocean, Southern Ocean, Australia, and North America, with Australia in particular much cooler (around  $3^{\circ}\text{C}$  below the LM projection) during 2081-2100. NN-GPR - EA differences are broadly similar, with the west coast of South America additionally predicted to be much cooler than EA (around  $4 - 6^{\circ}\text{C}$  below the EA projection). The Middle East / North Africa notably contradicts the general trend, with NN-GPR predicting around  $2.5^{\circ}\text{C}$  hotter Sahara desert than LM during 2081-2100. NN-GPR also predicts Asia and the Andes mountains as relatively hotter.

Figure 7b shows the relative differences in PR between NN-GPR’s projections and LM and EA. The largest differences occur near the intertropical convergence zone (ITCZ) and the



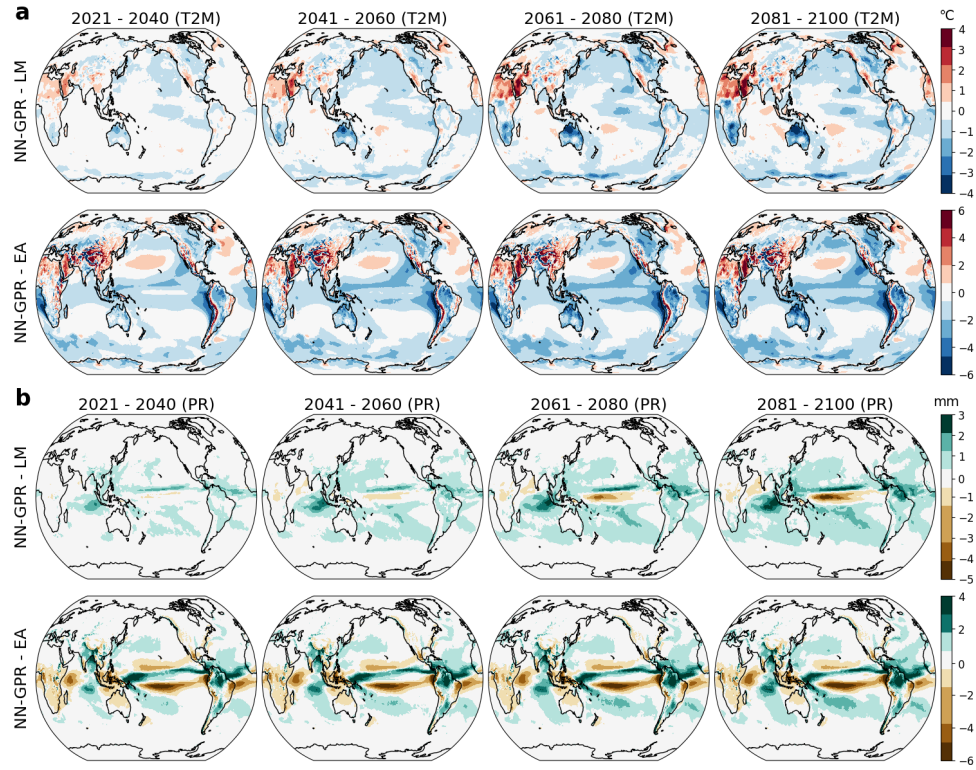


FIG 7. Spatial differences between NN-GPR's projections and LM's and EA's projections averaged over two-decade blocks. Panel (a) – T2M differences between NN-GPR and LM (top row) and NN-GPR and EA (bottom row). Red areas indicate NN-GPR projects higher temperatures, while blue areas indicate lower temperatures. Panel (b) – PR differences between NN-GPR and LM (top row) and NN-GPR and EA (bottom row). Green areas mean NN-GPR projects higher precipitation, and brown areas mean NN-GPR projects lower precipitation.

Indian ocean, with large swathes of minor differences in the surrounding oceans compared to LM and EA. There are almost no significant differences between any methods' projections outside the tropics. Within the tropics, NN-GPR projects significantly more precipitation than LM after 2060. Differences between NN-GPR and EA are relatively constant, except that NN-GPR gradually projects higher precipitation in northern South America and the South Pacific.

Notably, NN-GPR projects much lower average precipitation in the equatorial mid-Pacific than EA or LM. A drier mid-Pacific is consistent with the relatively increased precipitation seen elsewhere, particularly near southeast Asia and Northern South America, under La Niña like conditions (Lenssen, Goddard and Mason, 2020). Because we use a relatively small ensemble (16 members), some of the EA differences in PR may be due to the single outlying model (MCM-UA-1-0), as seen in Figure 6c.

**5.2. Regional climate projections.** One of the critical benefits of NN-GPR is that low resolution climate models are converted into a high resolution prediction akin to statistical downscaling. To evaluate NN-GPR's downscaling effectiveness, we compare our regional predictions (based on global inputs) against LM predictions and regional climate models (RCMs) average of North America. The RCM output comes from the NA-CORDEX simulations (Mearns et al., 2017), and we consider T2M and PR. We use CanESM2 projections down-scaled via CRCM5-OUR and CanRCM4. Initially, we considered GFDL-ESM2M down-scaled via CRCM5-OUR as well, but the projections were different enough from CanESM2

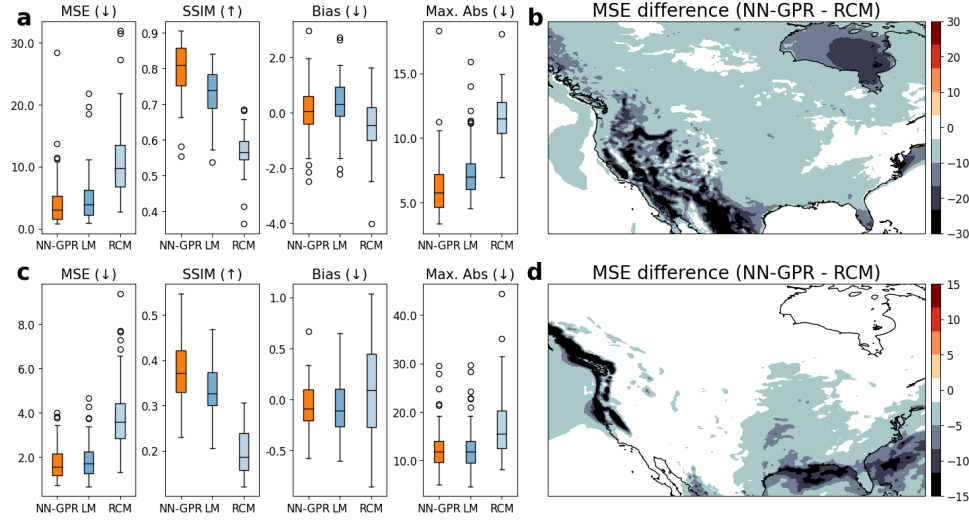


FIG 8. Skill metrics for NN-GPR, LM and the regional climate model average (RCM) for T2M (a) and PR (c) forecasting over 2015-2021. Max Abs. refers to the absolute largest difference between the forecast and the reanalysis field. Arrows indicate whether higher (↑) or lower (↓) numbers are better. Panels (b) and (d) – spatial MSE differences (NN-GPR - RCM) of T2M (a) and PR (c) projection.

to significantly blur the average fields. We evaluate each method on its ability to predict a small six year interval (2015-2021) test set of reanalysis fields, sliced to North America.

Figure 9a, c shows the MSE, the mean difference (Bias), the maximum absolute difference (Max Abs.), and SSIM scores of each method (NN-GPR, LM, and RCM) in predicting the test set (2015-2021) reanalysis fields for T2M and PR, respectively. NN-GPR has the lowest average MSE and highest average SSIM (MSE: 4.14, SSIM: 0.80) compared to the RCM (MSE: 10.92, SSIM: 0.57) and LM (MSE: 4.98, SSIM: 0.73). NN-GPR is, therefore, more accurate than either LM or RCM, meaning that it improves over both statistical and climatological downscaling approaches at a greatly reduced computational cost. The Bias and Max Abs. Boxplots display the average and maximum absolute difference between the prediction and the observation. NN-GPR yields nearly unbiased estimates of the mean (Bias: 0.01 °C) and greatly improved extreme estimation (Max Abs.: 6.21 °C) compared to the RCM (Bias: -0.43 °C, Max Abs.: 11.62 °C) and LM (Bias: 0.29 °C, Max Abs.: 7.51 °C). Thus, NN-GPR also captures the target process’s average behavior and extremal behavior better than either method.

Figures 9b, d show the temporally averaged MSE differences between NN-GPR and the RCM mean to show where NN-GPR provides improvement. NN-GPR has nearly uniformly smaller MSE values for T2M, with considerable improvements in the western United States and northern Mexico. Therefore, NN-GPR may capture interannual variability and topographic effects better than the RCM average. There are similarly large decreases in MSE in the Hudson Bay and the Chesapeake Bay for T2M in the Pacific Northwest and near Florida for PR. These widespread improvements suggest that NN-GPR can surpass the historical skill of RCM’s, particularly in regions of high variability. Thus, NN-GPR may offer a practical and computationally inexpensive surrogate for RCM ensembles, which are often used to assess extreme behavior (Mearns et al., 2017; Haugen et al., 2018). Because there is significantly less tradeoff between spatial resolution and computational cost compared to RCMs, we could cheaply study extreme behavior at fine scales.

Figure 9a, b shows the yearly spatial averages of each method’s predictions of North American T2M and PR fields. Strikingly, we see a convergence of the NN-GPR and RCM predic-

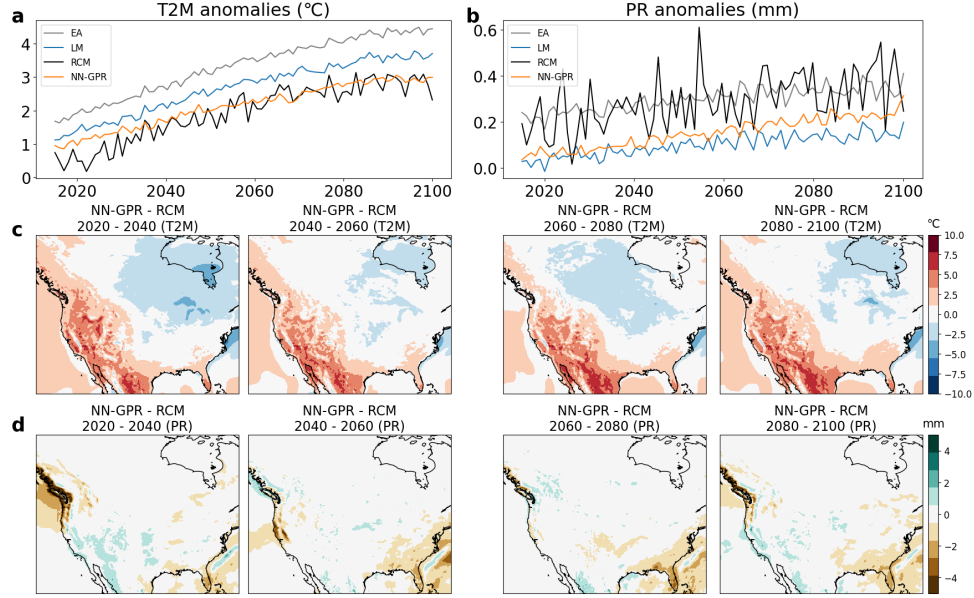


FIG 9. Panels (a) and (b) – yearly average anomaly projection (with respect to the 1950-2015 average) for each method and the RCM mean for T2M and PR. For T2M, NN-GPR closely tracks the RCM anomalies, while being consistently lower than RCM in PR. Panels (c) and (d) – spatial differences between the NN-GPR and RCM mean for T2M (c) and PR (d).

tions around 2040, with near total agreement by 2070. Despite the large differences early on (Figure 8), the two methods broadly agree near the end of the projection period. This sheds new light on the global predictions in Figure 6 and suggests that NN-GPR may be acting as a global downscaling model in addition to a forecasting model. Comparing the NN-GPR predictions with the EA predictions in Figure 9a, we can again see that NN-GPR runs cool which is consistent with Figure 6. For PR (Figure 9b), our model projects a slightly drier climate than either the RCM or EA, although the rate of precipitation increase is projected to be higher.

Figure 9c shows that the early differences between NN-GPR and the RCM might be due to NN-GPR projecting a warmer Pacific. After 2060, the differences between the two models stabilize (Figure 9a), albeit with NN-GPR consistently predicting a significantly warmer western United States and slightly cooler Canada and Hudson Bay. Differences in PR (Figure 9d) are essentially negligible save for in the Pacific Northwest and the Southeast, where NN-GPR projects a significantly drier climate. These differences largely account for the consistent gap between NN-GPR and the RCM in Figure 9b.

One of the critical benefits of our approach is that no RCM is required to produce predictions at RCM resolutions that are on par with RCM quality. RCMs introduce new uncertainties and biases, require subjective decision making, and have substantial computing requirements. Our NN-GPR method does not require any interpolation, does not average out the features of individual models, and is relatively cheap to compute, making it well suited to even larger ensembles than considered here. The results in Figure 8 show that NN-GPR is an adequate stand-in for RCM prediction and can even improve over small ensembles of RCMs for some climate variables like T2M. This could be beneficial for estimating climate impacts in regions with little RCM coverage.

**6. Discussion.** We proposed a Gaussian process regression (GPR) based on deep neural network kernels (Lee et al., 2017), called NN-GPR, to improve spatiotemporal climate model

integration. NN-GPR predicts reanalysis fields based on ensembles of climate model output, which constitutes an integration of the climate models. Because NN-GPR uses a deep neural network kernel, the predictions approximate the predictions of a fully trained deep neural network with an equivalent architecture. However, NN-GPR allows us to quantify predictive uncertainty through the usual GPR prediction equations (Equation 2). Our NN-GPR approach radically departs from traditional model weighting integration schemes since we dispense with model weights and instead consider posterior predictive means as integrations. That is, we treat model integration as a prediction problem rather than a mixture weight estimation problem.

The simulation results in Sections 4.1 and 4.2 showed that our proposed NN-GPR approach was more accurate than ensemble averaging and regression. However, our method had slightly more conservative uncertainty quantification than weighted ensemble averaging and was comparable to regression. We showed that NN-GPR represented uncertainty better in high variance regions, such as over land for surface temperatures. Table 1 showed that NN-GPR was most accurate early on in the T2M prediction interval and slowly deteriorated thereafter. We found that this was due to covariate shift in the distribution of T2M model ensembles (Figure 4) under SSP245, causing the variance of the predictions to increase (Figure 2). For PR, our method was consistently more accurate than the existing approaches. This was likely due to the significantly smaller covariate shift in the PR model ensembles.

The reanalysis results in section 5 showed that NN-GPR greatly improved over ensemble averaging and moderately improved over pointwise linear regression. NN-GPR was found to produce similar overall global and regional mean predictions as the ensemble mean but significantly improved the fine-scale detail, such as in mountainous regions (Figure 1, 8). These numerous local improvements reduced MSE and increased SSIM, particularly in high variance regions. Looking further at the local level, we found that NN-GPR projections were highly competitive with RCM projections. NN-GPR consistently estimated North American T2M and PR fields with higher accuracy and fidelity (Figure 9).

Through extensive testing, we found that NN-GPR is sensitive to covariate shift (Figure 3). When the distribution of the inputs (climate model ensemble) in the prediction period is different from the training period, NN-GPR can have an inflated prediction variance. Another potential limitation of our approach is that we use an NNGP kernel based on densely connected neural networks, rather than convolutional networks (Garriga-Alonso, Rasmussen and Aitchison, 2018) or recurrent networks (Alemohammad et al., 2020). Convolutional NNGP kernels could improve our method’s ability to synthesize spatial information, while recurrent kernels could help explicitly account for temporal information. Imposing these relational structures has been shown to help with generalization (Battaglia et al., 2018).

Finally, the uncertainty quantification abilities of our model are relatively primitive since they only provide a single variance value for each field-wise prediction. Theoretically, our model could be extended to incorporate spatially varying uncertainty, which may improve prediction and uncertainty quantification. However, computationally, this would make likelihood evaluation prohibitively expensive since we could no longer use the Kronecker product shortcut for matrix inversion (Section A).

The simulation results in Sections 4.1 and 4.2 showed that NN-GPR is most accurate when the test data are relatively similar to the training data, i.e., in the near future rather than the far future. This suggests that the NN-GPR approach could be quite powerful in weather prediction, where vast quantities of high-frequency training data are available, and predictions only need to be made over short time horizons (a few days). In future work, we will explore the scalability of the NN-GPR approach to high-frequency weather data and evaluate its competitiveness against leading finite width deep learning approaches.

**Funding.** B. Li’s research is partially supported by NSF-DMS-1830312 and NSF-DMS-2124576. R. Sriver was partially supported by the U.S. Department of Energy, Office of Science, Biological and Environmental Research Program, Earth and Environmental Systems Modeling, MultiSector Dynamics, Contracts No. DE-SC0016162 and DE-SC0022141.

## APPENDIX A: PARAMETER ESTIMATION

We use  $\theta = \{\sigma_w^2, \sigma_b^2\}$  to denote the weight and bias variances in the neural network, and  $\phi = \{\theta, \sigma^2\}$  to denote the full parameter collection including the error variance. For simplicity, and without loss of generality, we will assume  $X\beta$  is zero. Because we further assume  $\phi$  is shared across all spatial locations and all locations are independent, we can write the joint distribution over  $Y_i(p)$  for all  $i \in 1, \dots, n$  and  $p \in 1, \dots, d$ , as

$$(8) \quad N(0, \Sigma(\theta)_{n \times n} \otimes I_d + \sigma^2 I_{nd}),$$

where  $\otimes$  denotes the Kronecker product. To maximize the likelihood, we take the negative log-likelihood, which is proportional to

$$(9) \quad \mathcal{L}(\phi, D) = \frac{1}{2} Y^T K^{-1}(\phi) Y + \frac{1}{2} \log |K(\phi)|.$$

For most practical problems, the dimension of the reanalysis fields,  $d$ , is too large to compute the true  $nd \times nd$  covariance matrix  $K(\phi)$ , let alone invert  $K(\phi)$ . However, we can avoid unnecessary computations and make matrix inversion manageable by exploiting the block diagonal structure of the covariance matrix. That is, We can make evaluations of  $\mathcal{L}(\phi, D)$  tractable by using the fact that

$$\begin{aligned} K(\phi) &= \Sigma(\theta) \otimes I_d + \sigma^2 I_{nd} \\ &= (\Sigma(\theta) + \sigma^2 I_n) \otimes I_d, \end{aligned}$$

since we assumed each location has the same noise distribution  $N(0, \sigma^2)$ . Therefore,  $K^{-1}(\phi) = (\Sigma(\theta) + \sigma^2 I_n)^{-1} \otimes I_d^{-1}$  and

$$Y^T K^{-1}(\theta) Y = \sum_p Y_p^T (\Sigma(\theta) + \sigma^2 I_n)^{-1} Y_p,$$

where  $Y_p$  is a  $1 \times n$  vector consisting of the  $p$ ’th location in each of the  $n$  reanalysis fields. For our model integration problem,  $n$  is typically small enough ( $n < 1000$ ) to quickly invert the  $n \times n$  matrix  $(\Sigma(\theta) + \sigma^2 I_n)$ . Similarly, we use  $K(\phi) = (\Sigma(\theta) + \sigma^2 I_n) \otimes I_p$ , to get

$$\begin{aligned} \log |K(\phi)| &= \log |(\Sigma(\theta) + \sigma^2 I_n) \otimes I_p| \\ &= p \log |\Sigma(\theta) + \sigma^2 I_n| + n \log |I_p| \\ &= p \log |\Sigma(\theta) + \sigma^2 I_n|. \end{aligned}$$

These two manipulations result in an equivalent loss function (to equation 9)

$$(10) \quad \mathcal{L}(\phi, D) = \sum_p Y_p^T (\Sigma(\theta) + \sigma^2 I_n)^{-1} Y_p + p \log |\Sigma(\theta) + \sigma^2 I_n|,$$

with a significantly lower memory cost.

The loss in Equation 10 does not readily admit closed-form solutions for any parameter in  $\theta$ . However, for some common activation functions, such a ReLU or Tanh,  $\mathcal{L}(\theta, D)$  can be differentiated with respect to  $\theta$ , since  $\Sigma(\theta)$  is differentiable with respect to  $\theta$ . We can, therefore, apply gradient descent or any of its variants to find local minimizers  $\hat{\theta}$ . Stochastic



gradient descent is also possible with mini-batching performed over the  $p$  locations rather than the  $n$  samples.

Optimizing the prior, rather than setting it, is crucial since, as shown in (Lee et al., 2017), the two priors determine how well the neural network  $\Phi_A(\cdot, \theta)$  can learn. The variance parameters and the activation function define a phase space, with large regions corresponding to poor predictive performance. Manually setting the parameter values is precarious since the critical region where training can occur can be small and shrinks with increasing depth. We optimize their values to locate this critical region to help ensure our model (Equation 7) has low approximation and generalization error.

## REFERENCES

- ABRAMOWITZ, G., HERGER, N., GUTMANN, E., HAMMERLING, D., KNUTTI, R., LEDUC, M., LORENZ, R., PINCUS, R. and SCHMIDT, G. A. (2019). ESD Reviews: Model dependence in multi-model climate ensembles: weighting, sub-selection and out-of-sample testing. *Earth System Dynamics* **10** 91–105.
- ALEMOHAMMAD, S., WANG, Z., BALESTRIERO, R. and BARANIUK, R. (2020). The recurrent neural tangent kernel. *arXiv preprint arXiv:2006.10246*.
- ARORA, S., DU, S. S., LI, Z., SALAKHUTDINOV, R., WANG, R. and YU, D. (2019). Harnessing the Power of Infinitely Wide Deep Nets on Small-data Tasks. In *International Conference on Learning Representations*.
- BATTAGLIA, P. W., HAMRICK, J. B., BAPST, V., SANCHEZ-GONZALEZ, A., ZAMBALDI, V., MALINOWSKI, M., TACCHETTI, A., RAPOSO, D., SANTORO, A., FAULKNER, R. et al. (2018). Relational inductive biases, deep learning, and graph networks. *arXiv preprint arXiv:1806.01261*.
- BHAT, K. S., HARAN, M., TERANDO, A. and KELLER, K. (2011). Climate projections using Bayesian model averaging and space–time dependence. *Journal of agricultural, biological, and environmental statistics* **16** 606–628.
- BORNN, L., SHADDICK, G. and ZIDEK, J. V. (2012). Modeling nonstationary processes through dimension expansion. *Journal of the American Statistical Association* **107** 281–289.
- BOWMAN, K. W., CRESSIE, N., QU, X. and HALL, A. (2018). A Hierarchical Statistical Framework for Emergent Constraints: Application to Snow-Albedo Feedback. *Geophysical Research Letters* **45** 13–050.
- BRACEGIRDLE, T. J. and STEPHENSON, D. B. (2012). Higher precision estimates of regional polar warming by ensemble regression of climate model projections. *Climate dynamics* **39** 2805–2821.
- CHANDLER, R. E. (2013). Exploiting strength, discounting weakness: combining information from multiple climate simulators. *Philosophical Transactions of the Royal Society A: Mathematical, Physical and Engineering Sciences* **371** 20120388.
- EYRING, V., BONY, S., MEEHL, G. A., SENIOR, C. A., STEVENS, B., STOUFFER, R. J. and TAYLOR, K. E. (2016). Overview of the Coupled Model Intercomparison Project Phase 6 (CMIP6) experimental design and organization. *Geoscientific Model Development* **9** 1937–1958.
- FLATO, G., MAROTZKE, J., ABIODUN, B., BRACONNOT, P., CHOU, S. C., COLLINS, W., COX, P., DRI-OUUECH, F., EMORI, S., EYRING, V. et al. (2014). Evaluation of climate models. In *Climate change 2013: the physical science basis. Contribution of Working Group I to the Fifth Assessment Report of the Intergovernmental Panel on Climate Change* 741–866. Cambridge University Press.
- GARRIGA-ALONSO, A., RASMUSSEN, C. E. and AITCHISON, L. (2018). Deep convolutional networks as shallow gaussian processes. *arXiv preprint arXiv:1808.05587*.
- GHAFARIANZADEH, M. and MONTELEONI, C. (2013). Climate Prediction via Matrix Completion. In *AAAI (Late-Breaking Developments)*.
- GIORGI, F. and MEARN, L. O. (2002). Calculation of average, uncertainty range, and reliability of regional climate changes from AOGCM simulations via the “reliability ensemble averaging”(REA) method. *Journal of Climate* **15** 1141–1158.
- GIORGI, F. and MEARN, L. O. (2003). Probability of regional climate change based on the Reliability Ensemble Averaging (REA) method. *Geophysical research letters* **30**.
- GIORGI, F., RAFFAELE, F. and COPPOLA, E. (2019). The response of precipitation characteristics to global warming from climate projections. *Earth System Dynamics* **10** 73–89.
- GLECKLER, P. J., TAYLOR, K. E. and DOUTRIAUX, C. (2008). Performance metrics for climate models. *Journal of Geophysical Research: Atmospheres* **113**.
- GNEITING, T. and RAFTERY, A. E. (2007). Strictly proper scoring rules, prediction, and estimation. *Journal of the American statistical Association* **102** 359–378.
- GOODFELLOW, I., BENGIO, Y. and COURVILLE, A. (2016). *Deep learning*. MIT press.

- GREENE, A. M., GODDARD, L. and LALL, U. (2006). Probabilistic multimodel regional temperature change projections. *Journal of Climate* **19** 4326–4343.
- HAUGEN, M. A., STEIN, M. L., MOYER, E. J. and SRIVER, R. L. (2018). Estimating changes in temperature distributions in a large ensemble of climate simulations using quantile regression. *Journal of CLIMATE* **31** 8573–8588.
- HERSBACH, H., BELL, B., BERRISFORD, P., HIRAHARA, S., HORÁNYI, A., MUÑOZ-SABATER, J., NICOLAS, J., PEUBEY, C., RADU, R., SCHEPERS, D. et al. (2020). The ERA5 global reanalysis. *Quarterly Journal of the Royal Meteorological Society* **146** 1999–2049.
- KATZFUSS, M. (2017). A multi-resolution approximation for massive spatial datasets. *Journal of the American Statistical Association* **112** 201–214.
- KNUTTI, R., FURRER, R., TEBALDI, C., CERMAK, J. and MEEHL, G. A. (2010). Challenges in combining projections from multiple climate models. *Journal of Climate* **23** 2739–2758.
- KNUTTI, R., SEDLÁČEK, J., SANDERSON, B. M., LORENZ, R., FISCHER, E. M. and EYRING, V. (2017). A climate model projection weighting scheme accounting for performance and interdependence. *Geophysical Research Letters* **44** 1909–1918.
- LAMBERT, S. J. and BOER, G. J. (2001). CMIP1 evaluation and intercomparison of coupled climate models. *Climate Dynamics* **17** 83–106.
- LEE, J., BAHRI, Y., NOVAK, R., SCHOENHOLZ, S. S., PENNINGTON, J. and SOHL-DICKSTEIN, J. (2017). Deep neural networks as gaussian processes. *arXiv preprint arXiv:1711.00165*.
- LENSSSEN, N. J., GODDARD, L. and MASON, S. (2020). Seasonal Forecast Skill of ENSO Teleconnection Maps. *Weather and Forecasting* **35** 2387–2406.
- MACKAY, D. J. (1992). A practical Bayesian framework for backpropagation networks. *Neural computation* **4** 448–472.
- MEARNS, L., MCGINNIS, S., KORYTINA, D., ARMITT, R., BINER, S., BUKOVSKY, M., CHANG, H., CHRISTENSEN, O., HERZMANN, D., JIAO, Y. et al. (2017). The NA-CORDEX dataset, version 1.0. *NCAR Climate Data Gateway. Boulder (CO): The North American CORDEX Program* **10** D6SJ1JCH.
- NEAL, R. M. (2012). *Bayesian learning for neural networks* **118**. Springer Science & Business Media.
- NORTH, G. R., BELL, T. L., CAHALAN, R. F. and MOENG, F. J. (1982). Sampling errors in the estimation of empirical orthogonal functions. *Monthly weather review* **110** 699–706.
- O’NEILL, B. C., TEBALDI, C., VUUREN, D. P. v., EYRING, V., FRIEDLINGSTEIN, P., HURTT, G., KNUTTI, R., KRIEGLER, E., LAMARQUE, J.-F., LOWE, J. et al. (2016). The scenario model intercomparison project (ScenarioMIP) for CMIP6. *Geoscientific Model Development* **9** 3461–3482.
- RÄISÄNEN, J., RUOKOLAINEN, L. and YLHÄISI, J. (2010). Weighting of model results for improving best estimates of climate change. *Climate dynamics* **35** 407–422.
- RASMUSSEN, C. and WILLIAMS, C. (2006). *Gaussian Processes for Machine Learning. Adaptive Computation and Machine Learning*. MIT Press, Cambridge, MA, USA.
- ROUGIER, J., GOLDSTEIN, M. and HOUSE, L. (2013). Second-order exchangeability analysis for multimodel ensembles. *Journal of the American Statistical Association* **108** 852–863.
- SANSOM, P. G., STEPHENSON, D. B. and BRACEGIRDLE, T. J. (2017). On constraining projections of future climate using observations and simulations from multiple climate models. *arXiv preprint arXiv:1711.04139*.
- SHAND, L. and LI, B. (2017). Modeling nonstationarity in space and time. *Biometrics* **73** 759–768.
- SHIMODAIRA, H. (2000). Improving predictive inference under covariate shift by weighting the log-likelihood function. *Journal of statistical planning and inference* **90** 227–244.
- SMITH, R. L., TEBALDI, C., NYCHKA, D. and MEARNS, L. O. (2009). Bayesian modeling of uncertainty in ensembles of climate models. *Journal of the American Statistical Association* **104** 97–116.
- TEBALDI, C. and KNUTTI, R. (2007). The use of the multi-model ensemble in probabilistic climate projections. *Philosophical transactions of the royal society A: mathematical, physical and engineering sciences* **365** 2053–2075.
- TEBALDI, C., MEARNS, L. O., NYCHKA, D. and SMITH, R. L. (2004). Regional probabilities of precipitation change: A Bayesian analysis of multimodel simulations. *Geophysical Research Letters* **31**.
- TRENBERTH, K. E. (2011). Changes in precipitation with climate change. *Climate Research* **47** 123–138.
- WANG, Z. and BOVIK, A. C. (2002). A universal image quality index. *IEEE signal processing letters* **9** 81–84.
- WILSON, A. G. and IZMAILOV, P. (2020). Bayesian deep learning and a probabilistic perspective of generalization. *arXiv preprint arXiv:2002.08791*.